



# The effects of nitrogen ionization during preparation and oxygen pressure during annealing on the morphology, structure, and luminescent properties of Mg-doped ZnO thin films

Jing Luo<sup>1</sup> · Hongyu Liu<sup>1</sup> · Weijie Deng<sup>1</sup> · Rengang Zhang<sup>1</sup>

Received: 15 April 2024 / Accepted: 7 June 2024 / Published online: 18 June 2024  
© The Author(s), under exclusive licence to Springer-Verlag GmbH Germany, part of Springer Nature 2024

## Abstract

In order to understand the effects of nitrogen ionization during preparation and oxygen pressure during annealing (OPA) on the morphology, structure, and luminescent properties of Mg-doped ZnO thin films,  $\text{Zn}_{0.97}\text{Mg}_{0.03}\text{O}$  films were prepared in both ionized and non-ionized  $\text{N}_2$  using Pulsed Laser Deposition (PLD), followed by annealing at 600 °C under various oxygen pressures. X-ray Diffraction (XRD) results reveal that all  $\text{Zn}_{0.97}\text{Mg}_{0.03}\text{O}$  films exhibit a preferentially oriented hexagonal wurtzite structure along the (002) direction, with the films prepared in ionized nitrogen showing the presence of  $\text{Zn}_3\text{N}_2$  phase. Field Emission Scanning Electron Microscopy (FESEM) observations indicate that the films prepared in non-ionized and ionized  $\text{N}_2$  exhibit near-spherical and conical shaped particles, respectively. Combined XRD and X-ray Photoelectron Spectroscopy (XPS) analyses indicate an increase in Zn interstitial ( $\text{Zn}_i$ ) content in the films after annealing, with higher content observed at a higher OPA; films annealed under oxygen pressure of 100 Pa exhibit maximum tensile stress and highest N content. Photoluminescence (PL) spectra of both ionized and non-ionized films reveal a strong ultraviolet-violet peak (360–450 nm) and weaker blue-green peak (450–550 nm), with a broad and weak near-infrared (NIR) peak around 825 nm. The NIR peak primarily originates from the recombination of electrons bound to  $\text{Zn}_i$  and holes bound to oxygen vacancies ( $\text{V}_o$ ); ionization of nitrogen enhances the green emission.

**Keywords** ZnO thin films · Mg doping · Oxygen pressure during annealing · Nitrogen ionization · Morphology · Luminescent properties

## 1 Introduction

ZnO is a direct wide-bandgap semiconductor material with a significant exciton binding energy, holding promising applications in thin-film transistors [1], solar cells [2], photocatalysis [3], and other fields. Current research and development efforts are focused on nanostructured forms and eco-friendly fabrication methods of ZnO [4, 5]. However, its intrinsic defects, such as Zn interstitials ( $\text{Zn}_i$ ) and oxygen vacancies ( $\text{V}_o$ ), exhibit self-compensation effects, resulting in its natural n-type semiconductor behavior. To enable the application

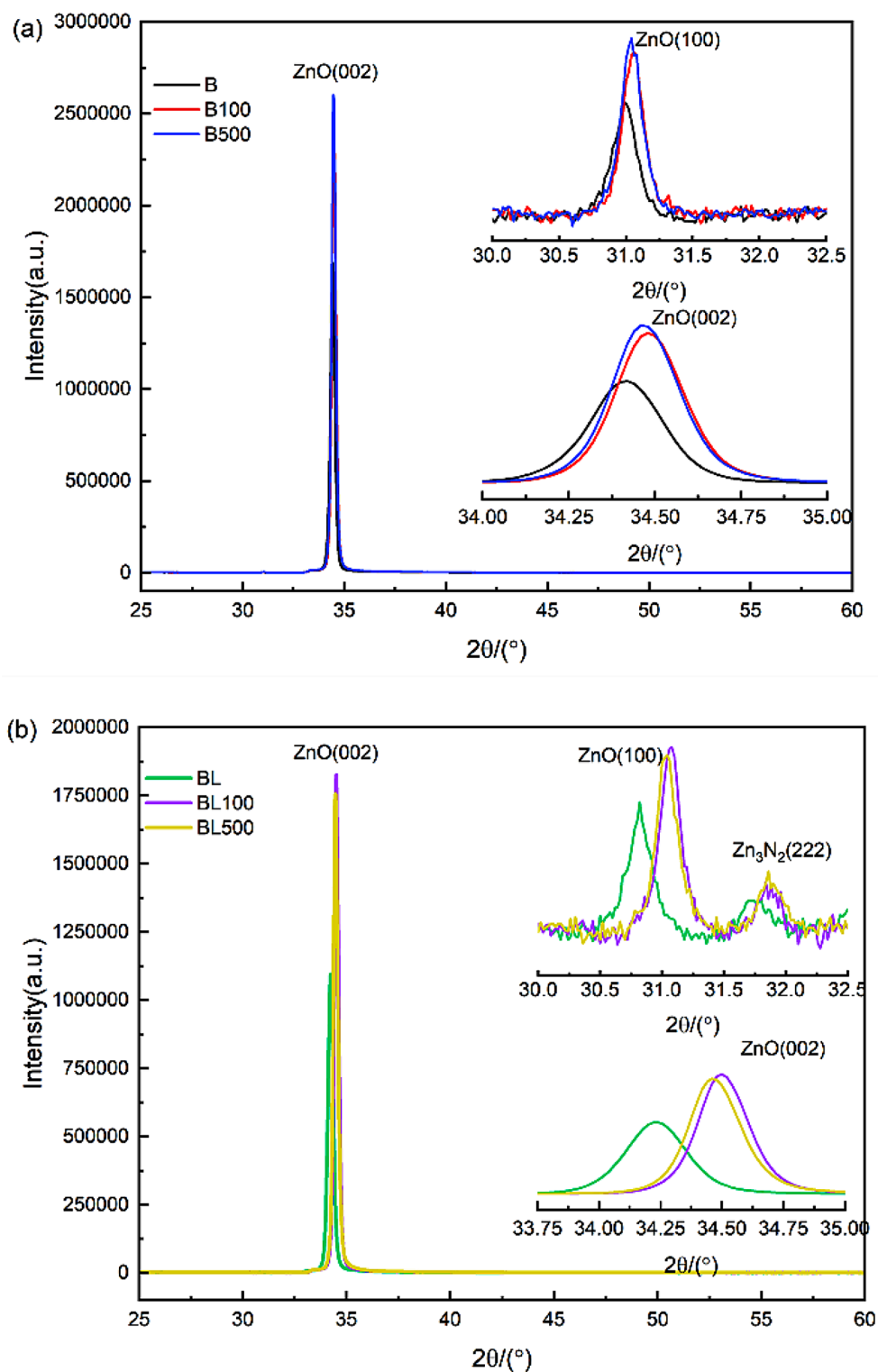
of ZnO semiconductors in optoelectronics, extensive research has focused on doping with Group I–V elements to tailor the types and concentrations of intrinsic defects, modulate the bandgap width, and form p-type ZnO films, thereby improving their electrical and optical properties [6, 7].

Jindal et al. [8] prepared different N-doped ceramic targets by mixing pure ZnO with  $\text{Zn}_3\text{N}_2$ , introducing N into the ZnO lattice via Pulsed Laser Deposition (PLD) in an oxygen environment. Due to nitrogen's lower electronegativity compared to oxygen, N occupies O sites, forming Zn–N bonds with Zn, which exhibit lower ionization energy than Zn–O bonds, introducing new acceptor levels above the valence band edge, resulting in a reduced optical bandgap of ZnO: N films. Martín-Tovar et al. [9] mixed pure ZnO powder with a superglue primarily containing ethyl cyanoacrylate (ECA) to form targets, and introduced N into the ZnO thin film lattice

✉ Hongyu Liu  
liuhongyu@wust.edu.cn

<sup>1</sup> Department of Applied Physics, School of Science, Wuhan University of Science and Technology, Wuhan 430065, China

**Fig. 1** XRD spectra of the non-ionized (a) and ionized (b) samples



using a Nd: YAG laser, passivating Vo while inducing outward relaxation, leading to lattice contraction. Wang et al. [10] used pure ZnO targets and Ar-N<sub>2</sub> mixed gas as the working gas, deposited Zn<sub>3</sub>N<sub>2</sub> films on substrates at 150 °C via DC magnetron sputtering, and annealed them in air or O<sub>2</sub> at 350–550 °C to transform them into

transparent ZnO films. It was found that p-type ZnO films could be obtained when annealed in air or O<sub>2</sub> at temperatures below 500 °C. However, the films reverted to n-type when annealed above 500 °C due to reduced N incorporation. Chang et al. [11] prepared ZnO films on glass substrates via magnetron sputtering and used a DC plasma

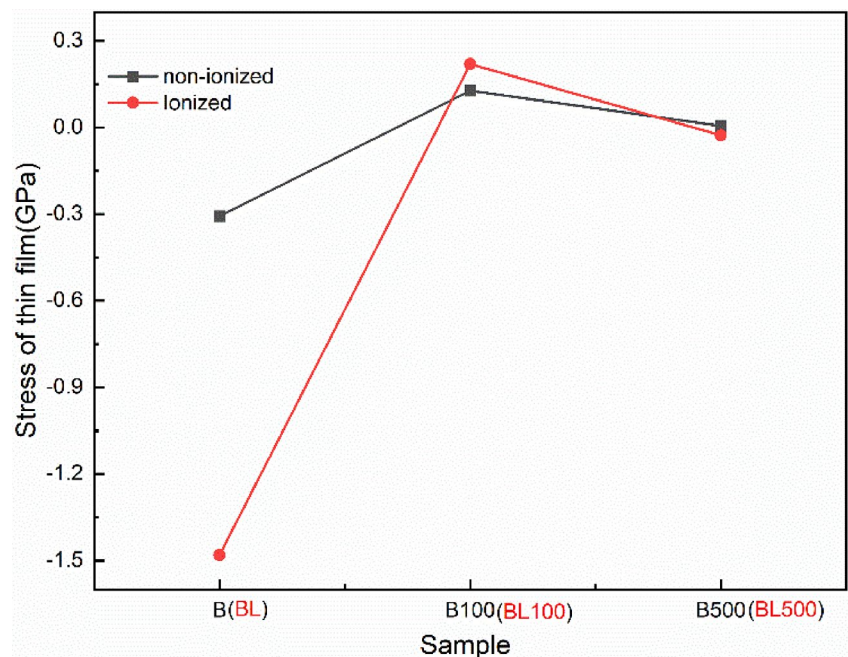
**Table 1** Lattice Parameters of ionized and non-ionized samples

Sample no.	Diffraction angle $2\theta / (^{\circ})$		Interplanar spacing $d / \text{\AA}$		Lattice parameters / $\text{\AA}$	Stress / GPa
	(100)	(002)	(100)	(002)	c	$\sigma$
B	31.00	34.41	2.885	2.607	5.214	-0.31
B100	31.05	34.47	2.880	2.602	5.204	0.13
B500	31.04	34.45	2.881	2.603	5.207	0.01
BL	30.83	34.23	2.901	2.620	5.240	-1.48
BL100	31.08	34.49	2.878	2.601	5.202	0.22
BL500	31.03	34.45	2.882	2.604	5.207	-0.03

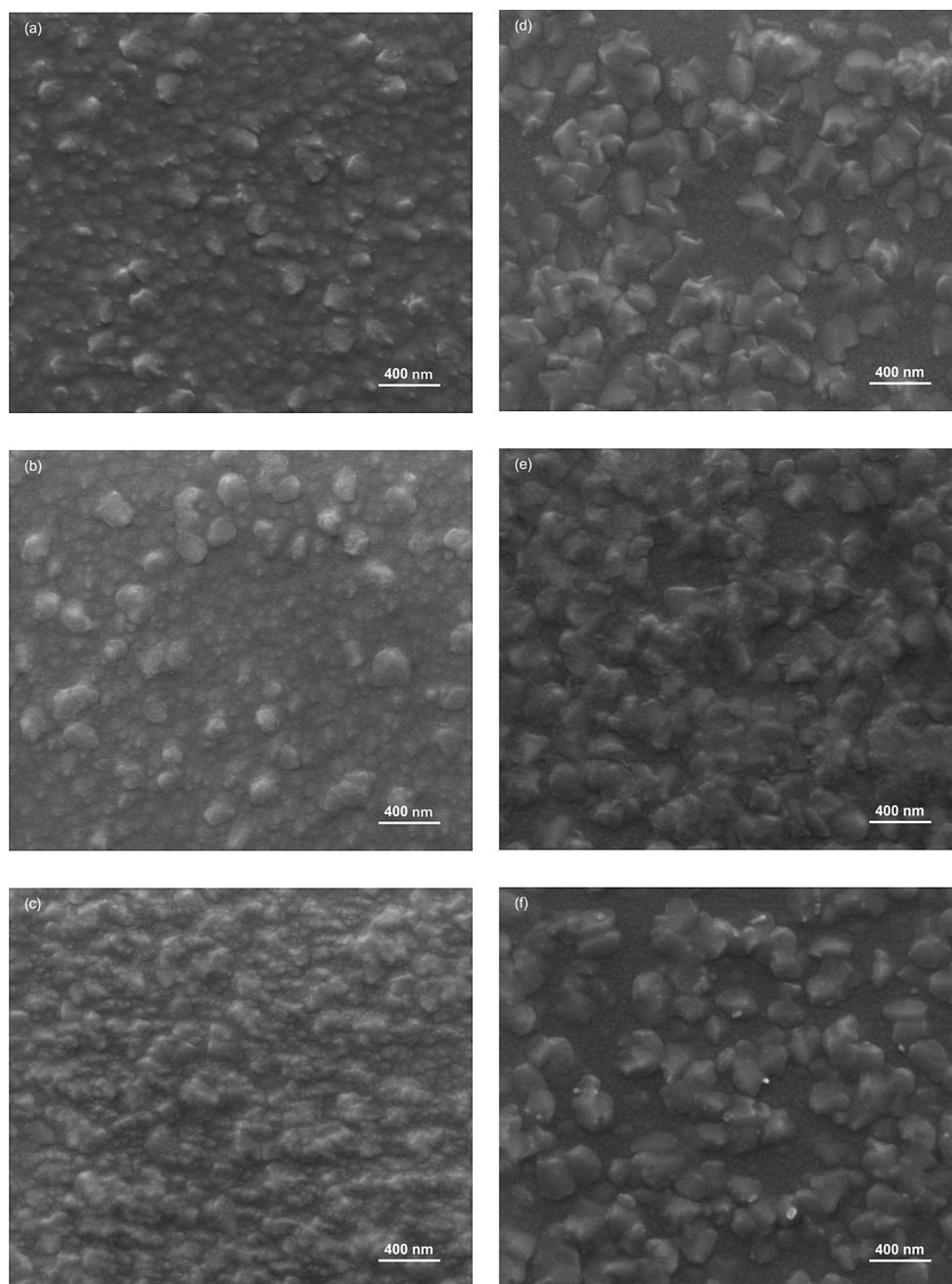
system to enhance N dissociation. The  $N_2/(Ar + N_2)$  flow ratio varied from 0 to 0.7 during the deposition process to investigate its effect on the properties of the ZnO films. Simeonov et al. [12] deposited N-doped ZnO films in an N-containing atmosphere, followed by rapid annealing in  $N_2$  at 400 °C and 550 °C. The results indicated that annealing at 400 °C resulted in n-type conductivity, while annealing at 550 °C resulted in p-type conductivity. In previous literature, experimental studies on incorporating N into ZnO via PLD using ionized  $N_2$  are lacking in the literature.

During the process of thin film fabrication, oxygen plays a crucial role in determining the structural morphology and properties of ZnO films. Currently, many researchers have investigated the influence of oxygen pressure on the morphology, structure, and performance of thin films during the fabrication process. Min et al. [13] investigated the effect of oxygen partial pressure on the Fermi level of  $ZnO_{1-x}$  films, finding that reducing the oxygen pressure from 10 to 3.3 Pa upshifted the Fermi level of ZnO films by 0.6 eV. This indicates significant changes in the energy balance and electronic structure of oxygen-deficient ZnO films. Pandey et al. [14] deposited

ZnO films using a dual ion beam sputtering deposition system under different oxygen partial pressures at a constant temperature of 400 °C. With increasing oxygen partial pressure, the crystallinity of the films decreased, and the  $V_o$  decreased. Ma et al. [15] investigated the effects of different oxygen pressures on the morphology, structure, and properties of ZnO: Ti films using RF magnetron sputtering, observing that increasing oxygen pressure enhanced the (002) diffraction peak intensity of the films while gradually reducing the optical bandgap. Some researchers have also studied the effects of annealing in oxygen atmosphere on ZnO films. Kumar et al. [16] studied the influence of annealing in  $O_2$  at 700 °C for different times on the structural and morphological properties of ZnO films, finding that with increasing annealing time, the film roughness and grain size increased. Hsu et al. [17] investigated the effects of oxygen annealing on the structure and optoelectronic properties of Al-doped ZnO films, discovering that oxygen annealing could eliminate  $V_o$  and improve the crystal structure. Additionally, they also studied the effect of air annealing on the properties of Al-doped ZnO thin films prepared by the high-speed atmospheric atomic layer deposition (AALD) method and

**Fig. 2** Variation of stress within the samples

**Fig. 3** SEM images of the non-ionized samples (a, B; b, B100; c, B500) and ionized samples (d, BL; e, BL100; f, BL500)



found that annealing temperatures below 600 °C mainly reduce the  $V_o$  acting as donors, while higher annealing temperatures above 600 °C could further reduce the mid-gap states [18]. In previous studies, there have been

**Table 2** Peak parameters of Zn 2P 1/2, Zn 2P 3/2 and Mg 1s (eV)

Sample	Zn 2p 1/2	Zn 2p 3/2	Mg 1s
B	1044.46	1021.39	1303.54
B100	1044.69	1021.51	1303.72
B500	1044.57	1021.45	1303.98
BL	1044.40	1021.28	1303.63
BL100	1044.57	1021.45	1304.02
BL500	1044.63	1021.51	1304.03

no reports on the influence of oxygen pressure during annealing (OPA) on the structure and properties of thin films. Researchers have only reported the effects of oxygen pressure or flow rate during the film deposition process on the structure and properties of the films [19, 20]. The change of OPA has not only the change of oxygen flow but also the change of pressure, which will affect the change of stress and defects after film deposition and also the doping of N. Therefore, it is necessary to investigate the effect of changing OPA on the films.

In this study, homemade Mg-doped ZnO targets were used to prepare  $Zn_{0.97}Mg_{0.03}O$  thin films via PLD in an

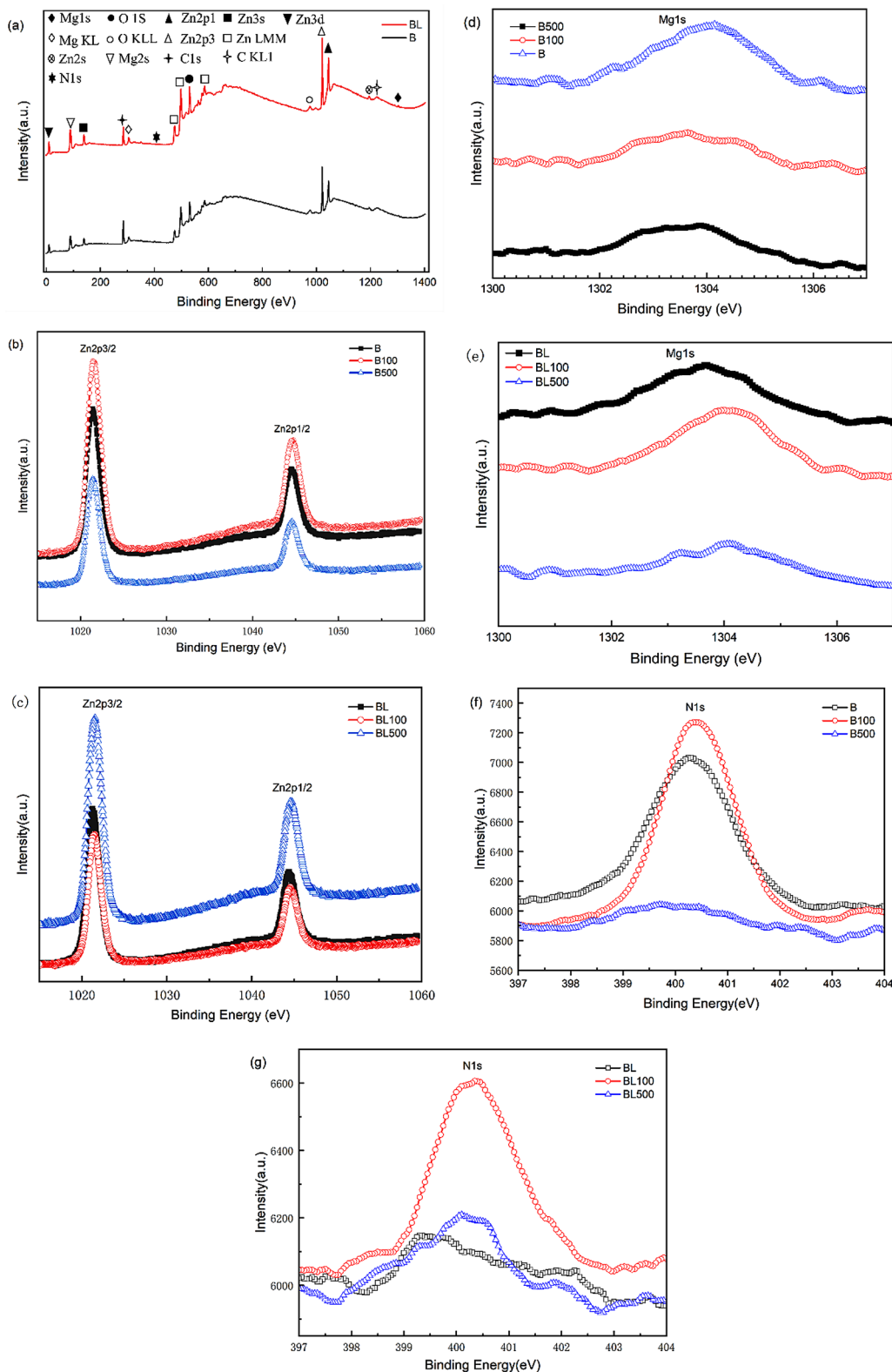


**Fig. 4** XPS survey spectrum (a), Zn 2P (b, non-ionized; c, ionized), Mg 1s (d, non-ionized; e, ionized), and N1s (f, non-ionized; g, ionized) spectra

ionized N<sub>2</sub>, followed by thermal annealing under different oxygen pressures. The effects of ionized nitrogen and OPA

on the structure and optical properties of Zn<sub>0.97</sub>Mg<sub>0.03</sub>O thin films were investigated.

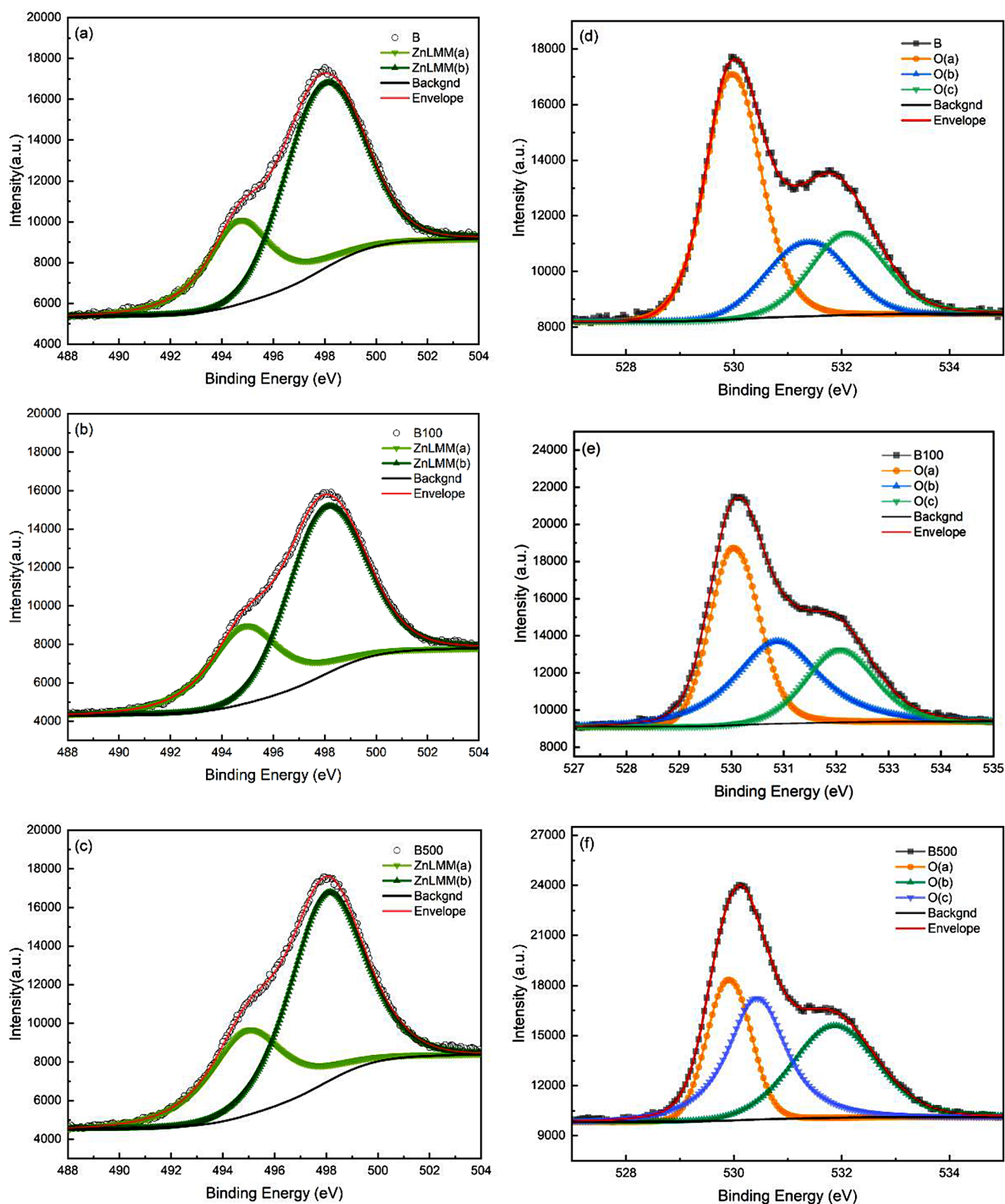
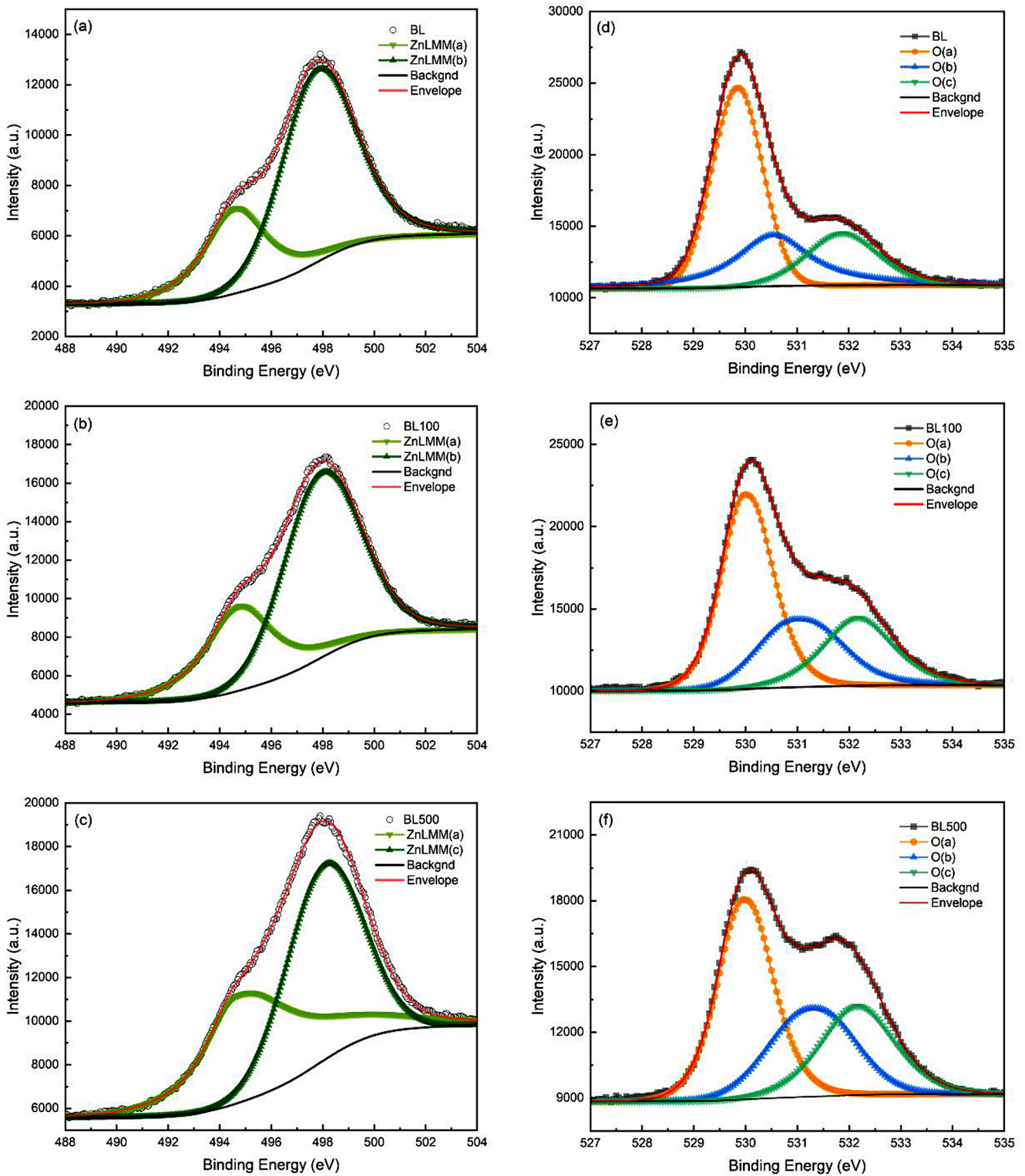


Fig. 5 Lorentz-Gaussian fitting spectra of non-ionized sample Zn LMM (a, B; b, B100; c, B500) and O 1s (d, B; e, B100; f, B500)

## 2 Experimental materials and methods

### 2.1 Target and film preparation



**Fig. 6** Lorentz-Gaussian fitting spectra of ionized samples Zn LMM (a, BL; b, BL100; c, BL500) and O 1s (d, BL; e, BL100; f, BL500)

The experiment was conducted in December 2023 at the PLD laboratory of the department of applied physics, school of science, Wuhan University of Science and Technology, China. High pure ZnO and MgO powders

with a purity of 99.99% were uniformly mixed, with a Mg doping concentration of 3 at%. The mixture was ground at 150 rpm for 120 min using an LGB04 ball mill to obtain homogeneity. The mixed powders were then

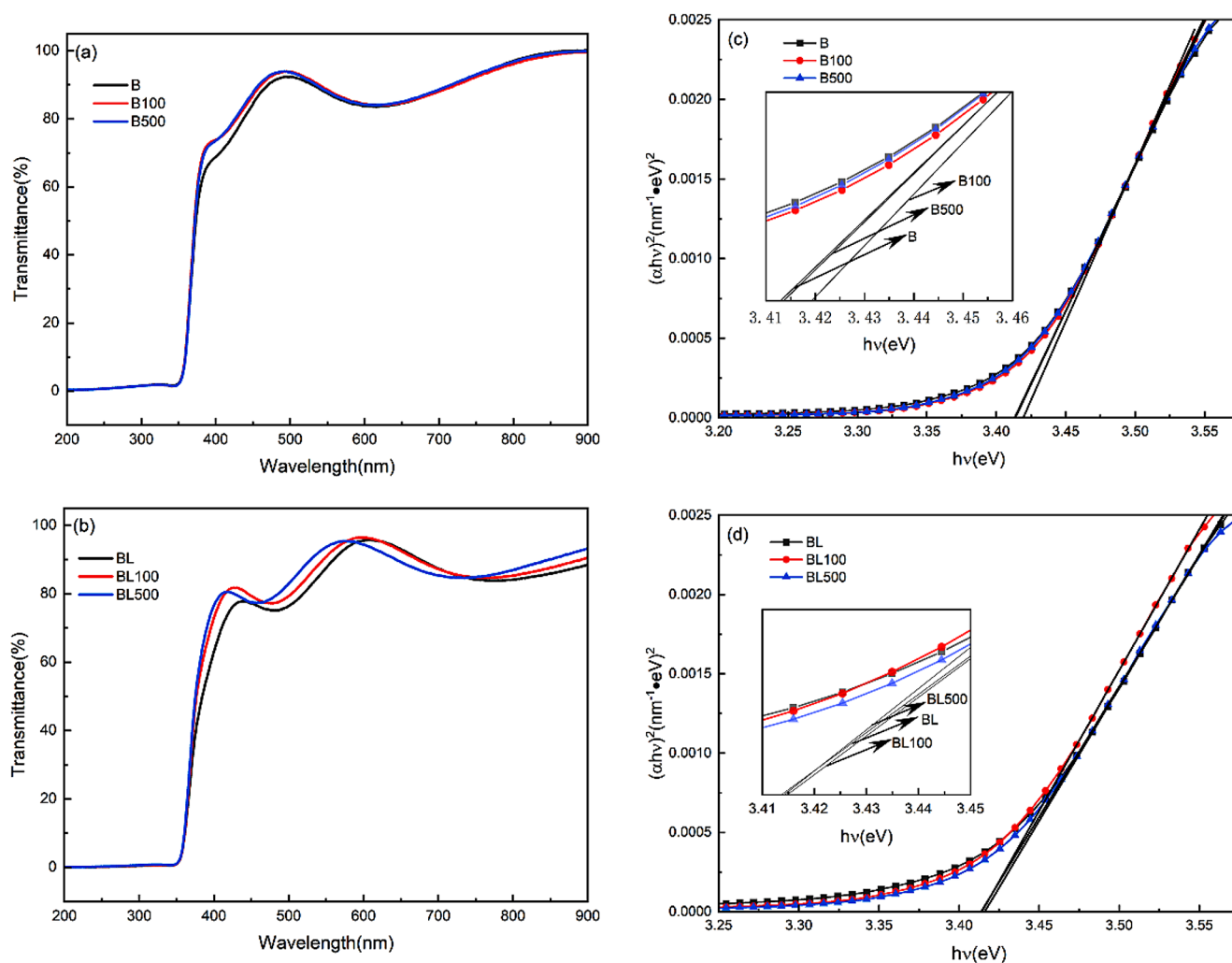


**Fig. 7** Transmission spectra of the samples (**a**, non-ionized; **b**, ionized) and  $E_g$  plotting method (**c**, non-ionized; **d**, ionized)

pressed into targets of 25 mm in diameter at room temperature using a YAW-1000D hydraulic press. The targets were sintered in an SX3-0-13 air resistance furnace following the sequence: 60 min ramping from room temperature to 200 °C, holding for 30 min; 90 min ramping to 600 °C, holding for 60 min; 50 min ramping to 850 °C, holding for 60 min; 100 min ramping to 950 °C, holding for 60 min; 60 min ramping to 1250 °C, holding for 300 min, and furnace cooling to room temperature.

Thin films were deposited using a PLD-450B system. Substrates of quartz glass were cleaned using an ultrasonic cleaner with distilled water, acetone, and alcohol solutions for 15 min each. After the cleaned substrates were dried, they were placed into the PLD chamber with a target-substrate distance of 95 mm. The chamber was evacuated to  $10^{-4}$  Pa and then filled with  $N_2$ , adjusting the flow rate to maintain a nitrogen pressure of around 0.9 Pa, with a substrate temperature of 500 °C. A 248 nm KrF excimer laser with a frequency of 5 Hz and a single

pulse energy of 300 mJ was used for deposition, with a pre-sputtering time of 10 min followed by deposition for 60 min. Deposition of the thin films was carried out under both ionized and non-ionized  $N_2$ , with ionized  $N_2$  voltage ranging from 0.25 to 0.27 kV and current from 0.28 to 0.35 mA.

The  $Zn_{0.97}Mg_{0.03}O$  thin films deposited by PLD were annealed under oxygen pressures of 100 Pa and 500 Pa using a quartz tube resistance furnace. The annealing process went as follows: ramping from room temperature to 600 °C for 192 min, holding for 120 min, and then furnace cooling to room temperature. The samples deposited under non-ionized  $N_2$  and annealed under oxygen pressures of 100 Pa and 500 Pa were labeled as B, B100, and B500, respectively. The samples deposited under ionized  $N_2$  and annealed under oxygen pressures of 100 Pa and 500 Pa were labeled as BL, BL100, and BL500, respectively.



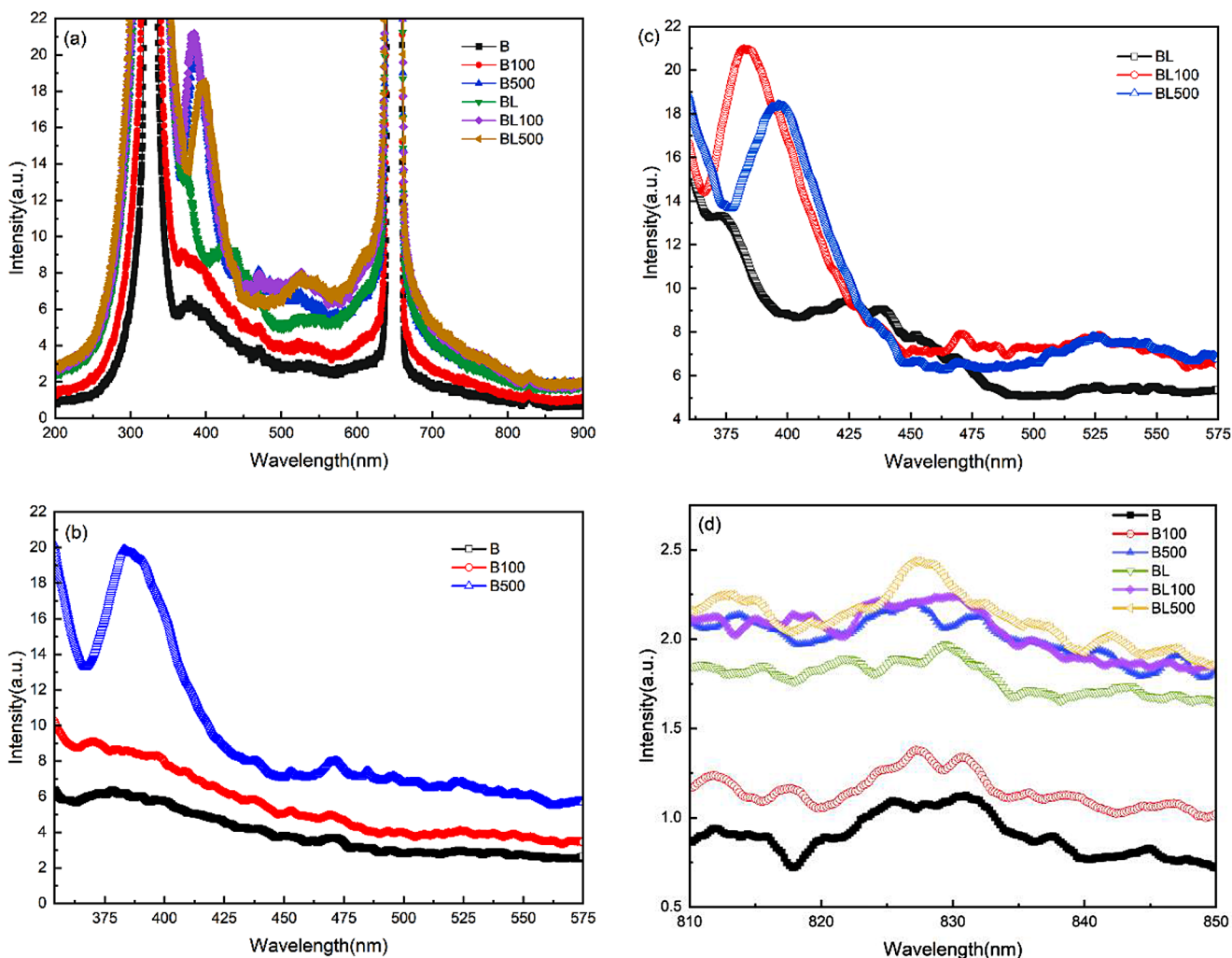


**Fig. 8** PL Spectra: (a) emission spectra of ionized and non-ionized samples in the range of 200–900 nm; (b) emission spectra of non-ionized samples in the range of 360–575 nm; (c) emission spectra of ion-

ized samples in the range of 360–575 nm; (d) NIR spectra of ionized and non-ionized samples

## 2.2 Characterization methods

The structural characterization of the prepared samples was conducted using a Rigaku SmartLab SE X-ray diffractometer (XRD) with Cu K $\alpha$  radiation. The scanning angle ( $2\theta$ ) ranged from 25 to 60°, with a scanning speed of 0.75°/min, a tube voltage of 40 kV, and a tube current of 40 mA. The surface morphology of the samples was observed using a FEI Nova Nano SEM400 field emission scanning electron microscope (FESEM). The thickness of the samples was measured using a spectroscopic ellipsometer (RC2, J. A. Woollam). The transmission spectra of the samples were measured using a UV-2550 UV-visible spectrophotometer (SHIMADZU). Chemical composition, chemical states, and molecular structures of the samples were analyzed using X-ray photoelectron spectroscopy (XPS) with an AXIS SUPRA+ instrument.

XPS data were processed using Avantage software, and peak fitting spectra were obtained using the Smart background and Lorentz-Gaussian fitting methods, with all data calibrated to the C 1s peak at 284.8 eV. The fluorescence spectra of the samples were measured using a Hitachi F-7000 fluorescence spectrophotometer with an excitation wavelength of 325 nm, emission wavelength range of 200–900 nm, scanning speed of 240 nm/min, excitation (emission) slit width of 2.5 (5.0) nm, and PMT voltage of 700 V.

**Table 3** Peak positions and area ratios of fitted peaks for non-ionized and ionized samples Zn LMM and O 1s

Sample	B	B100	B500	B	B100	B500
	Peak position(eV)			Area ratio (%)		
Zn LMM(a)-Zn <sub>i</sub>	494.67	494.88	494.93	29.64	31.94	33.36
Zn LMM(b)-Zn <sup>2+</sup>	497.93	498.02	498.02	70.36	68.06	66.64
O(a)- O <sup>2-</sup>	529.91	530.03	529.9	37.55	40.50	27.56
O(b)- Vo	530.5	530.88	530.4	23.24	35.48	35.89
O(c)-O <sub>i</sub>	531.83	532.07	531.87	39.20	24.02	36.55
Sample	BL	BL100	BL500	BL	BL100	BL500
	Peak position(eV)			Area ratio (%)		
Zn LMM(a)-Zn <sub>i</sub>	494.6	494.75	494.68	28.96	30.79	45.04
Zn LMM(b)-Zn <sup>2+</sup>	497.79	497.95	498.09	71.04	69.21	54.96
O(a)- O <sup>2-</sup>	529.77	529.98	529.94	43.94	48.92	44.24
O(b)- Vo	530.19	530.96	531.26	35.47	26.91	28.57
O(c)-O <sub>i</sub>	531.86	532.17	532.16	20.60	24.17	27.19

### 3 Results and discussion

#### 3.1 Structure and morphology

##### 3.1.1 XRD

The XRD pattern of the non-ionized sample is shown in Fig. 1(a). The diffraction peaks coincide with ZnO (JCPDS NO.36-1451), indicating the hexagonal wurtzite structure of ZnO with preferential growth along the c-axis (002) direction. No diffraction peaks corresponding to other substances were detected, confirming the sample's structure as hexagonal wurtzite ZnO.

The 2θ angles of (002) for B, B100, and B500 are 34.40°, 34.47°, and 34.45°, respectively, while those of (100) are 31.00°, 31.05°, and 31.04°, respectively. With increasing OPA, the 2θ angles of both (100) and (002) peaks show a trend of initially increasing and then decreasing. The interplanar spacing (d) and lattice constant (c) calculated according to the formulas (1) to (3) for the hexagonal close-packed (HCP) lattice are listed in Table 1. HCP lattice constant calculation formulas [21, 22]:

$$\left(\frac{1}{d}\right)^2 = \frac{4}{3} \left( \frac{h^2 + k^2 + hk}{a^2} \right) + \frac{l^2}{c^2} \quad (1)$$

$$a = \frac{2}{\sqrt{3}} d_{100} \quad (2)$$

$$c = 2d_{002} \quad (3)$$

Figure 1 (b) illustrates the XRD spectrum of the ionized sample. Apart from the (002) and (100) diffraction peaks corresponding to ZnO, a weaker diffraction peak at 2θ approximately 31.74° corresponding to the (222) plane of Zn<sub>3</sub>N<sub>2</sub> (JCPDS NO.04-004-2196) is observed in both pre-annealed and post-annealed ionized samples. Zn<sub>3</sub>N<sub>2</sub> is

formed during the film deposition process when ionized N<sub>2</sub> produces N ions that combine with Zn ions in ZnO. The parameters of the ZnO diffraction peaks for the ionized sample are also listed in Table 1, showing similar variation trends in the 2θ angles of the ZnO (002) and (100) diffraction peaks as observed in the non-ionized sample. From Table 1, it can be observed that the lattice constants (c) of both non-ionized and ionized samples exhibit a trend of initially decreasing and then increasing with increasing OPA. Lattice constants are influenced by Mg doping concentration, internal defects, and stress within the film [23]. Li et al. [24] proposed that the reduction in ZnO lattice constants and the shift of the (002) diffraction peak towards higher angles during annealing are caused by the release of residual stress. Shin et al. [25] suggested that the decrease in the c-axis lattice parameter after oxygen annealing is attributed to the occurrence of oversaturation of adsorbed atoms during the sputtering process, leading to competition between nucleation and aggregation, resulting in tensile strain along the a-axis direction in the ZnO film. There are mainly two types of film stress [16]: intrinsic stress caused by impurities and defects within the crystal, and extrinsic stress caused by lattice mismatch, growth conditions, and mismatch in thermal expansion coefficients between the film and substrate. The stress within the film can be calculated using the biaxial strain model (Eq. 4) [16, 26]:

$$\sigma = \frac{2C_{13}^2 - C_{33}(C_{11} + C_{12})}{2C_{13}} \cdot \frac{c - c_0}{c_0} \quad (4)$$

The elastic constants C<sub>11</sub>, C<sub>12</sub>, C<sub>13</sub>, and C<sub>33</sub> for single crystal ZnO have numerical values of 208.8, 119.7, 104.2, and 213.8 GPa, respectively [26]. c<sub>0</sub> (5.20661 Å) represents the lattice constant of stress-free ZnO powder. The lattice constants of the samples, denoted as c, were calculated and are presented in Table 1. The calculated

film stresses from Table 1 are plotted in Fig. 2, illustrating the variation trends of stress within the samples.

The non-ionized sample B experiences compressive stress (-0.31 GPa). After annealing in O<sub>2</sub>, both B100 and B500 experience tensile stress (0.13 GPa and 0.01 GPa, respectively), which decreases with increasing OPA. Similarly, the ionized sample BL also experiences compressive stress (-1.48 GPa). After annealing in O<sub>2</sub>, BL100 experiences tensile stress (0.22 GPa), while BL500 experiences a smaller compressive stress (-0.03 GPa). From Fig. 2, it is evident that both non-ionized and ionized samples exhibit a trend of increasing stress followed by decreasing stress. Conversely, lattice constants show a trend of decreasing followed by increasing, indicating that lattice constants decrease with increasing stress (positive values denote tensile stress, while negative values denote compressive stress) within the film.

### 3.1.2 SEM

Figure 3 (a) to (c) depict the surface morphology images of the non-ionized sample. The sample B exhibits a few white protruding particles. After annealing in O<sub>2</sub>, the white protruding particles in B100 become noticeably larger and more abundant, likely due to the secondary preferred orientation of the (002) crystal planes during annealing in O<sub>2</sub> [27]. The particles in the B500 sample appear dispersed, possibly due to the reduction in tensile stress during annealing at an oxygen pressure of 500 Pa. Figure 3 (d) to (e) display the surface morphology images of the ionized sample. Compared to the non-ionized sample, the ionized sample exhibits a transition from approximately circular particles to conical particles. This transformation may be attributed to the presence of Zn<sub>3</sub>N<sub>2</sub> in the ionized sample, which weakens the contact aggregation of the ZnO within the film.

### 3.1.3 XPS

Figure 4 (a) presents the XPS survey spectra confirming that the main components of both ionized and non-ionized samples are Zn, O, and Mg, with trace amounts of N and C. The presence of C is attributed to slight surface contamination in the experiment. Figure 4 (b) to (g) display the Zn 2P, Mg 1s, and N 1s spectra of the non-ionized and ionized samples. In the non-ionized sample B, two strong peaks appear at 1021.39 eV and 1044.46 eV, corresponding to the Zn 2p 3/2 and Zn 2p 1/2 peaks, respectively, with a binding energy (BE) gap of 23.07 eV. The ionized sample BL exhibits peaks at 1021.28 eV and 1044.40 eV for the Zn 2p 3/2 and Zn 2p 1/2 peaks, respectively, with a BE gap of 23.12 eV. These BE gaps closely resemble

those of pure ZnO (23.10 eV) [28], indicating that Zn in the films prepared with both non-ionized and ionized N<sub>2</sub> primarily exists in the form of Zn-O bonds. As evident from the peak position parameters of Zn 2P in Table 2, both B and BL show a shift towards higher BE for Zn 2p and Mg 1s after annealing in oxygen. Wang et al. [29] suggest that Mg, with a lower electronegativity than Zn, is more prone to losing electrons and forming Mg-O bonds with O. The shift towards higher BE of Zn 2p 3/2 and Zn 2p 1/2 after annealing is attributed to the increased opportunity for more O to enter the lattice and form Mg-O bonds under oxygen pressures of 100 Pa and 500 Pa. Similar observations were made by Goktas et al. [30], whose study indicated that annealing promotes the formation of Zn-O-Mg bonds in Mg-doped ZnO films, leading to an increase in the oxidation state within the film and a decrease in the valence electron density, resulting in a shift of the Zn 2p peaks towards higher BE.

From Fig. 4 (f) and (g), it can be observed that both ionized and non-ionized samples exhibit the strongest N 1s peak on the film surface after annealing under an oxygen pressure of 100 Pa, indicating the highest N content. This phenomenon may arise from metastable N ions substituting for O ions in the ZnO lattice, forming unstable acceptor N<sub>O</sub>. N<sub>O</sub> then attracts another N ion to form (N<sub>2</sub>)<sub>O</sub> donors. During annealing at elevated temperatures, (N<sub>2</sub>)<sub>O</sub> gains enough energy to diffuse out of the O ion sites in the ZnO lattice [31], resulting in an increase in surface N content of the annealed film. The maximum tensile stress of the film during annealing at an oxygen pressure of 100 Pa (Fig. 2) is most conducive to the departure of (N<sub>2</sub>)<sub>O</sub> from the O ion sites, thus leading to a higher N content and the highest intensity of the N 1s peak.

Figure 5 shows the Lorentz-Gaussian fitting graphs of non-ionized sample Zn LMM and O 1s, with the peak positions and area ratios listed in Table 3. The Zn LMM peak is divided into two peaks, Zn LMM(a) and Zn LMM(b), located at approximately 494 eV and 498 eV, respectively. The Zn LMM(a) peak is primarily associated with intrinsic defects Zn<sub>i</sub> in the film, while the Zn LMM(b) peak corresponds to Zn<sup>2+</sup> ions on the ZnO lattice [32, 33]. The O 1s peak is divided into three peaks, O(a), O(b), and O(c). O(a) is related to O<sup>2-</sup> ions on the ZnO lattice [1], O(b) is associated with Vo defects in the film [1, 34], and O(c) is related to O<sub>i</sub> defects and surface-adsorbed O in the film [35]. With increasing OPA, the area ratio of Zn LMM (a) related to Zn<sub>i</sub> in the non-ionized sample gradually increases. The area ratio of O (b) related to Vo defects also increases gradually. The area ratio of the defect peak O (a) related to O<sub>i</sub> decreases first and then increases. According to Table 3, the proportion

of  $O^{2-}/Zn^{2+}$  in B100 is the largest among B, B100, and B500 samples, indicating its best crystalline quality.

Figure 6 illustrates the Lorentz-Gaussian fitting spectra of ionized sample Zn LMM and O 1s. Similarly, Zn LMM is fitted into two peaks, Zn LMM (a) and Zn LMM (b), while O 1s is fitted into three peaks, O (a), O (b), and O (c). The relevant parameters for each fitting peak are listed in Table 3. With the increase of OPA, the proportion of peaks related to  $Zn_i$  in the ionized sample gradually increases, while the proportion of peaks related to  $O_i$  increases continuously, and the proportion of peaks related to  $V_O$  decreases first and then increases. Before annealing, the proportion of peaks related to  $O_i$  and  $Zn_i$  in the ionized sample (BL) is lower than that in the non-ionized sample (B), indicating that ionization is conducive to reducing the content of  $O_i$  and  $Zn_i$  in the sample. After annealing, except for  $Zn_i$  in BL500, the total area proportion of peaks related to  $V_O$  and  $O_i$  defects and the proportion of peaks related to  $Zn_i$  in the ionized sample are lower than those in the non-ionized sample, indicating that ionization is conducive to reducing the generation of internal defects in the film under certain OPA.

## 3.2 Optical performance analysis

### 3.2.1 Optical transmittance

Figure 7 shows the transmission spectra of the non-ionized (a) and ionized (b) samples. Both non-ionized and ionized samples exhibit good transmittance, with interference fringes observed in the transmittance curves, indicating that the films are thick and the surfaces are smooth and uniform [30]. Compared to the as-deposited samples, the transmittance curves of both non-ionized and ionized samples after annealing exhibit a slight blue shift in the absorption edge, with no significant change observed with increasing OPA. This may be attributed to annealing being more conducive to the incorporation of  $Mg^{2+}$  into the ZnO lattice [26], and the difference in electronegativity between  $Mg^{2+}$  and  $Zn^{2+}$  causing the blue shift in the absorption edge [36]. The optical bandgap  $E_g$  of the films is calculated using the Tauc equation [37]:

$$(\alpha h\nu) = A(h\nu - E_g)^{1/2} \quad (5)$$

$$\alpha = \frac{\ln \frac{1}{T}}{L} \quad (6)$$

The absorption coefficient  $\alpha$  in the Tauc equation of Eq. (5), can be derived from Eq. (6) derived from the Beer Lambert equation. In Eq. (5) to (6),  $T$  is the transmittance,  $L$  is the thickness of the film,  $h$  is the Planck constant,  $A$  is a

constant,  $\nu$  is the frequency of the incident photons, and  $E_g$  is the optical bandgap. By plotting  $h\nu$  against  $(\alpha h\nu)^2$ , the  $E_g$  of the non-ionized and ionized samples is obtained using linear extrapolation, as shown in Fig. 7(c) and (d) respectively. The  $E_g$ s of the non-ionized samples B, B100, and B500, as well as the ionized samples BL, BL100, and BL500, are 3.4132 eV, 3.4171 eV, 3.4133 eV, 3.4167 eV, 3.4168 eV, and 3.4154 eV, respectively. The variation of  $E_g$  with OPA is consistent with the change in stress, showing a trend of increasing first and then decreasing. Therefore, stress variation is identified as the main factor affecting  $E_g$ . It is observed that both non-ionized and ionized samples exhibit the maximum  $E_g$  at 100 Pa OPA (3.4171 eV and 3.4168 eV, respectively).

### 3.2.2 PL spectrum

Figure 8 (a) depicts the PL spectra of the samples within the range of 200 to 900 nm. Both non-ionized and ionized samples exhibit a strong ultraviolet to violet peak (360 to 450 nm) and a weaker blue to green peak (450 to 550 nm) within the range of 360 to 575 nm. Additionally, a broad and weak NIR peak is observed near 825 nm. Previous studies by the authors have indicated that the ultraviolet emission is primarily caused by the radiative recombination of free excitons [38], while the violet emission peak near 385 nm arises from the radiative recombination of electrons trapped by Zn vacancies with holes in the conduction band (CB) [27]. Fang et al. [39] suggested that green light emission is caused by  $Vo$ , while Panigrahy et al. [40] demonstrated that green light emission originates from singly charged  $Vo^+$ ; when the defect hole is depleted within the thin film,  $Vo^+$  captures an electron from the CB to form a neutral center, leading to radiative recombination with holes in the valence band (VB), thus causing green emission. Figure 8(b) displays the emission spectrum of the non-ionized sample within the range of 360 to 575 nm. After B is annealed, the violet emission strengthens due to the increased  $Zn_i$  (Table 3), and this enhancement gradually increases with the elevation of OPA. However, the green emission near 525 nm is almost absent, which can be attributed to the difficulty of ionizing electrons from deep-level donor defects such as  $Vo$ . Figure 8(c) illustrates the emission spectrum of the ionized sample within the range of 360 to 575 nm. The violet intensity of BL increases after annealing at 100 Pa oxygen pressure and decreases when the OPA increases to 500 Pa. The green emission peak near 525 nm is enhanced after annealing and shows no significant variation with increasing OPA. Hence, it is inferred that ionization in this experiment promotes the formation of  $Vo^+$ , resulting in green emission from the ionized sample.

The author's previous research has identified three potential causes for red and NIR emission: (1) radiative recombination of electrons bound to  $Zn_i$  with holes bound to  $O_i$ ; (2) radiative recombination of electrons bound to  $V_o$  with holes in the VB [27]; (3) radiative transitions between  $Zn_i$  and  $V_o$  [41]. Figure 8(d) presents the NIR emission spectra of both non-ionized and ionized samples. It can be observed that the NIR emission intensities of both ionized and non-ionized samples increase with increasing OPA. Combining the XPS results, it is found that the variation in NIR intensity correlates with changes in the  $Zn_i$  content in the samples. When the OPA rises to 500 Pa, the  $Zn_i$  and  $O_i$  content in BL500 and B500 samples are nearly the highest, resulting in the strongest NIR emission. Therefore, it is inferred that the NIR emission of the samples is mainly due to the radiative recombination of electrons bound to  $Zn_i$  with holes bound to  $O_i$ .

## 4 Conclusion

By using the PLD method to prepare Mg-doped ZnO thin films  $Zn_{0.97}Mg_{0.03}O$  in  $N_2$  and investigating the influence of nitrogen ionization and OPA on the film's structural morphology and luminescent properties, the following main conclusions are drawn: the  $Zn_{0.97}Mg_{0.03}O$  samples prepared by non-ionization exhibit a hexagonal wurtzite structure with preferential growth along the (002) direction. In contrast, the samples prepared by ionization not only exhibit this structure but also generate a new phase of  $Zn_3N_2$ . Compared to non-ionization, ionization under certain OPA can reduce the defect content in the film and improve its crystallinity. After annealing at oxygen pressure, the  $Zn_i$  content increases, and it increases further with increasing OPA. At 100 Pa oxygen pressure annealing, the non-ionized and ionized samples exhibit the highest tensile stress and highest N content. The NIR peak observed in the PL spectra of the samples originates from the radiative recombination of electrons bound to  $Zn_i$  and holes bound to  $O_i$ .

**Author contributions** Hongyu Liu provided ideas and guided the design of research plans, and Jing Luo implemented the research process, collected and sorted out data and wrote a thesis. During the experiment, technical was supported by Rengang Zhang, Weijie Deng.

**Data availability** The data that support the findings of this study are available from the corresponding author, upon reasonable request.

## Declarations

**Conflict of interest** The authors declare that they have no conflicts of interest.

## References

1. B. Kim, D. Lee, B. Hwang, D.-J. Kim, C.K. Kim, *Mol. Cryst. Liq. Cryst.* **735**, 61–74 (2021)
2. W. Zhang, N. Tang, *Mater. Res. Express.* **7**, 105903 (2020)
3. M. Baradaran, F.E. Ghodsi, C. Bittencourt, E. Llobet, *J. Alloys Compd.* **788**, 289–301 (2019)
4. B.J.A. José, M.D. Shinde, *Sci. Rep.* **14**, 2310 (2024)
5. B.J.A. José, M.D. Shinde, C.A.C. Azuranahim, *Nanomater Energy.* **12**, 117–130 (2023)
6. S. Talu, S. Boudour, I. Bouchama, B. Astinchap, H. Ghanbaripour, M.S. Akhtar, S. Zahra, *Microsc. Res. Tech.* **85**, 1213–1223 (2022)
7. Y. Wang, J. Song, H. Zhang, X. Zhang, G. Zheng, J. Xue, B. Han, X. Meng, F. Yang, J. Li, *J. Alloys Compd.* **822**, 153688 (2020)
8. K. Jindal, M. Tomar, R.S. Katiyar, V. Gupta, *J. Appl. Phys.* **120**, 135305 (2016)
9. E.A. Martín-Tovar, E. Chan y Díaz, M. Acosta, R. Castro-Rodriguez, A. Iribarren, *Appl. Phys. A* **122**, 1–7 (2016)
10. C. Wang, Z. Ji, K. Liu, Y. Xiang, Z. Ye, *J. Cryst.* **259**, 279–281 (2003)
11. H.T. Chang, G.J. Chen, *Thin Solid Films.* **618**, 84–89 (2016)
12. S. Simeonov, A. Szekeres, D. Spassov, M. Anastasescu, I. Stanculescu, M. Nicolescu, E. Aperathitis, M. Modreanu, M. Gartner, *Nanomaterials.* **12**, 19 (2022)
13. C.H. Min, S. Cho, S.H. Lee, D.Y. Cho, W.G. Park, J.G. Chung, E. Lee, J.C. Lee, B. Anass, J.H. Lee, C.S. Hwang, S.J. Oh, *Appl. Phys. Lett.* **96**, 201907 (2010)
14. S.K. Pandey, S.K. Pandey, U.P. Deshpande, V. Awasthi, A. Kumar, M. Gupta, S. Mukherjee, *Semicond. Sci. Technol.* **28**, 085014 (2013)
15. L. Ma, X. Ai, X. Huang, S. Ma, *Superlattice Microst.* **50**, 703–712 (2011)
16. V. Kumar, V. Kumar, S. Som, A. Yousif, N. Singh, O.M. Ntwaeaborwa, A. Kapoor, H.C. Swart, *J. Colloid Interface Sci.* **428**, 8–15 (2014)
17. C.H. Hsu, X.P. Geng, W.Y. Wu, M.J. Zhao, P.H. Huang, X.Y. Zhang, Z.B. Su, Z.R. Chen, S.Y. Lien, *Mater. Sci. Semicond. Process.* **133**, 105929 (2021)
18. C.H. Hsu, X.P. Geng, W.Y. Wu, M.J. Zhao, X.Y. Zhang, P.H. Huang, S.Y. Lien, *Molecules.* **25**, 5043 (2020)
19. L. Radjehi, A. Djelloul, S. Lamri, M.F. Slim, M. Rahim, *Surf. Eng.* **35**, 520–526 (2019)
20. L. Wang, J. Liu, L. Zhao, X. Fan, Q. Wang, *Opt. Mater.* **122**, 111672 (2021)
21. F. Lekoui, S. Hassani, M. Ouchabane, H. Akkari, D. Dergham, W. Filali, E. Garoudja, *Braz J. Phys.* **51**, 544–552 (2021)
22. J. Kang, J. Yun, Y.-Y. Oh, S.-J. Kim, M. Kamiko, N.-H. Kim, J.-H. Koh, *J. Korean Ceram. Soc.* **59**, 742–748 (2022)
23. T.H. Kim, J.J. Park, S.H. Nam, H.S. Park, N.R. Cheong, J.K. Song, S.M. Park, *Appl. Sur Sci.* **255**, 5264–5266 (2009)
24. X. Li, Y. Wang, W. Liu, G. Jiang, C. Zhu, *Mater. Lett.* **85**, 25–28 (2012)
25. J.W. Shin, Y.S. No, J.Y. Lee, J.Y. Kim, W.K. Choi, T.W. Kim, *Appl. Sur Sci.* **257**, 7516–7520 (2011)
26. R. Cebulla, R. Wendt, K. Ellmer, *J. Appl. Phys.* **83**, 1087–1095 (1998)
27. J. Luo, H.Y. Liu, W.J. Deng, R.G. Zhang, C. He, *J. Mater. Sci.-Mater. El.* **34**, 2172 (2023)
28. L.C. Chao, S.J. Lin, W.C. Chang, *Nucl. Instrum. Meth B* **268**, 1581–1584 (2010)
29. M. Wang, J. Yi, S. Yang, Z. Cao, X. Huang, Y. Li, H. Li, *J. Zhong. Appl. Sur Sci.* **382**, 217–224 (2016)
30. A. Goktas, A. Tumbul, Z. Aba, M. Durgun, *Thin Solid Films.* **680**, 20–30 (2019)

31. S.S. Shinde, C.H. Bhosale, K.Y. Rajpure, J. Photochem. Photobiol B **113**, 70–77 (2012)
32. W. Li, L. Fang, G. Qin, H. Ruan, H. Zhang, C. Kong, L. Ye, P. Zhang, F. Wu, J. Appl. Phys. **117**, 145301 (2015)
33. D. Fang, C. Li, N. Wang, P. Li, P. Yao, Cryst. Res. Technol. **48**, 265–272 (2013)
34. P.T. Hsieh, Y.C. Chen, K.S. Kao, C.M. Wang, Appl. Phys. A **90**, 317–321 (2007)
35. F.H. Wang, M.S. Chen, Y.L. Jiang, H.W. Liu, T.K. Kang, J. Alloys Compd. **897**, 63174 (2022)
36. T. Zhang, Y. Wang, Z. Pan, Sol Energy. **184**, 570–583 (2019)
37. J. Varghese, S.K. Saji, N.R. Aswathy, R. Vinodkumar, Eur. Phys. J. Plus. **136**, 1–13 (2021)
38. M. Abdelkrim, M. Guezzoul, M. Bedrouni, M. Bouslama, A. Ouerdane, B. Kharroubi, J. Alloys Compd. **920**, 165703 (2022)
39. H.W. Fang, J.Y. Juang, S.J. Liu, Int. J. Nanotechnol. **14**, 992–1000 (2017)
40. B. Panigrahy, M. Aslam, D.S. Misra, M. Ghosh, D. Bahadur, Adv. Funct. Mater. **20**, 1161–1165 (2010)
41. S. Vempati, J. Mitra, P. Dawson, Nanoscale Res. Lett. **7**, 1–10 (2012)

**Publisher's Note** Springer Nature remains neutral with regard to jurisdictional claims in published maps and institutional affiliations.

Springer Nature or its licensor (e.g. a society or other partner) holds exclusive rights to this article under a publishing agreement with the author(s) or other rightsholder(s); author self-archiving of the accepted manuscript version of this article is solely governed by the terms of such publishing agreement and applicable law.